MDPI

Evolution of Ore-Forming Fluids and Gold Deposition of the Sanakham Lode Gold Deposit, SW Laos: Constrains from Fluid Inclusions Study

Shusheng Liu [1,2], Linnan Guo [2,*], Jun Ding [2], Lin Hou [2], Siwei Xu [2], Meifeng Shi [2], Huimin Liang [2], Fei Nie [3] and Xiaoyu Cui [4]

[1] College of Earth Sciences, Chengdu University of Technology, Chengdu 610059, China; cdlshusheng@163.com
[2] Chengdu Center, China Geological Survey, Chengdu 610081, China; 13980689100@163.com (J.D.); houlin_aaron@163.com (L.H.); xswxswxsw@163.com (S.X.); shimeifeng-1204@163.com (M.S.); lianghm_cugb@126.com (H.L.)
[3] Research Center of Applied Geology, China Geological Survey, Chengdu 610036, China; niefei_cugb@163.com
[4] Sichuan Zhuyu Investment Co., Ltd., Chengdu 610042, China; xy92159168@163.com
* Correspondence: linnanguo@163.com; Tel.: +86-028-82321057

Abstract: The Sanakham gold deposit is a newly discovered gold deposit in the Luang Prabang (Laos)–Loei (Thailand) metallogenic belt. It consists of a series of auriferous quartz-sulfide veins, which is distinguished from the regional known porphyry-related skarn and epithermal gold deposits. There are four mineralization stages identified in Sanakham, with native gold grains mainly occurring in stages II and III. Evolution of ore-forming fluids and gold deposition mechanisms in Sanakham are discussed based on fluid inclusion petrography, microthermometry, and Laser Raman spectroscopy. The original ore-forming fluids belong to a medium-high temperature (>345 °C) CH_4-rich CH_4–CO_2–NaCl–H_2O system. In stages II and III, the ore fluids evolve into a NaCl–H_2O–$CO_2 \pm CH_4$ system characterized by medium temperature (~300 °C), medium salinity (~10 wt% NaCl eq.), and CO_2-rich (~10% mol). They might finally evolve into a NaCl–H_2O system with temperature decreasing and salinity increasing in stage IV. Two fluid immiscibility processes occurred in stages II and III, which created high-CH_4 & low-CO_2 and low-CH_4 & high-CO_2 end-members, and CO_2-poor and CO_2-rich endmembers, respectively. Gold-deposition events are suggested to be associated with the fluid immiscibility processes, with P–T conditions and depth of 236–65 MPa, 337–272 °C, and 8.7–6.5 km, respectively.

Keywords: fluid inclusion; CH_4- and CO_2-rich ore fluids; fluid immiscibility; gold deposition; Sanakham gold deposit; Laos

1. Introduction

The mainland of Southeast Asia consists of a series of continental blocks or terranes together with related sutures and volcanic arcs (Figure 1a). It is endowed with a diversity of mineral resources distributed in several important metallogenetic belts, such as the Truong Son Fe-Cu-Au-W-Sn belt, Vientiane–Kon Tum K-Al-Cu-Au belt, Da Lat Au-Fe-Cu belt, Gulf of Thailand–East Malaysia Au-Sb-Cu belt, and the Luang Prabang–Loei Cu-Au-Ag belt [1]. The Luang Prabang (Laos)–Loei (Thailand) metallogenic belt lies along the western periphery of the Indochina Block, to the east of Changning–Menglian–Chieng Mai Suture zone (Figure 1a). The belt, formed during the subduction–accretionary orogeny of the Paleo-Tethys Ocean and the subsequent collisional orogeny between the Sibumasu Block and the Indochina Block, is traditionally recognized as a metallogenic belt dominated by porphyry-related skarn and epithermal deposits [2,3] (Figure 1b).

Figure 1. Regional geological map. (**a**) Simplified tectonic map showing structural units of Laos andadjacent regions; (**b**) simplified geological map of the Luang Prabang–Loei metallogenic belt (geochronological data from [4–16], modified from [5,10]). A = andesite; B = basalt; Br = breccia; D = dacite; Db = diabase; Dr = diorite; G = gabbro; Gd = Granodiorite; M = monzonite; R = rhyolite; T = tuff.

The Sanakham gold deposit, a newly discovered gold deposit in this belt with a gold resource of 10.6 t @ 3.05 g/t Au, is located about 3 km north to the Muang Sanakham County, southwest Laos (Figure 1b). The gold orebodies consist of a series of quartz-sulfide veins that are controlled by secondary structures of the regional NNE-trending brittle-ductile shear zone, which is different from the regional porphyry-related skarn and epithermal

gold deposits. Given it is such a particular lode gold deposit in the Luang Prabang–Loei belt, studying it should be meaningful in both prospecting and theory. Nevertheless, there are no reports of studies on the Sanakham gold deposit up to now. We therefore carried out detailed petrography, microthermometry, and Laser Raman spectroscopy on fluid inclusions in gold-related quartz from different mineralization stages, identified by field and microscopic observation. This study aims to discuss the evolution of ore-forming fluids and gold deposition mechanisms in Sanakham, and to provide basic data for further study on regional gold metallogenic regularity.

2. Geology and Mineralization

2.1. Regional Geological Setting

The Luang Prabang–Loei metallogenic belt is NNE-NE trending, bounded by the Dien Bien Phu–Loei Suture (DLS) to the east, the Nan–Uttaradit Suture (NUS) to the west, and the Meiping Fault (MPF) to the south, and is adjacent to the Simao Block in the Sanjiang Region to the north [1]. The NE-trending Luang Prabang tectonic belt develops in the central-northern part of the metallogenic belt (Figure 1a); it is characterized by a large number of Late Paleozoic–Mesozoic intermediate–basic magmatic rocks, including pillow-shaped basalts, andesites, gabbro, diabase, diorite, and volcanic clastic rocks (Figure 1b). The Carboniferous magmatic rocks, including basalt, andesite, and diabase, mainly occurred around Luang Prabang and Pak Lay [5–7]. The Permian to Early Triassic igneous rocks are normally gabbro, diabase, tuff, and diorite, and are confined around Luang Prabang and Xaignabouli [4,8–10]. The Middle–Late Triassic exposed intermediate–acid igneous rocks are widespread in the belt [5,9,11,12]. Some important gold deposits occurred in the Luang Prabang tectonic belt, including orogenic Au (Phapon [17,18]), skarn gold–copper (Pangkuam [19]), and the Sanakham lode gold deposit.

The northwest side of the Luang Prabang tectonic belt belongs to the Simao–Phitsanulok Block (Figure 1a), which is regarded as a back-arc foreland basin [1]. It mainly consists of Late Paleozoic sandstone, shale, and epimetamorphic rocks, Triassic clastic rocks and carbonate rocks, and Middle Jurassic red clastic rocks [10]. Only a few copper occurrences are found in the basin.

The southeast side of the Luang Prabang tectonic belt is the Loei Fold Belt (Figure 1a), with Late Paleozoic and Mesozoic sediments and volcanic rocks [6,13], as well as Early–Middle Triassic magmatic rocks exposed (Figure 1b). The representative porphyry–skarn copper–gold deposits (Phu Lon, Puthep, and Phu Thap Fah) develop to the north and northeast of Loei in Thailand and are genetically related with the felsic-intermediate intrusive rocks [14,15]. A set of Late Permian to Early Triassic andesitic–rhyolitic volcanic and pyroclastic rocks develops in the south of the metallogenic belt, associated with several epithermal Au–Ag deposits [16].
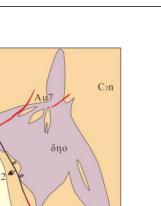
2.2. Local Geological Setting

The main stratum in the mining area is the Upper Carboniferous Nanpo Formation (C_2n), which consist of purple–red thick-layered metamorphic siltstone, silty slate, slate, and brown thin-layered feldspar–debris sandstone (Figure 2). It is N to NNE trending, generally dipped to the west with a dip angle of 60–85°, and is more than 600 m in thickness. The Quaternary sediments (Q), which mainly consists of fragments that came from slate, carbonaceous slate, and metamorphic siltstone, are widespread on gentle slopes and platforms in various areas of the mining area.

The structures in the mine are mainly brittle–ductile shear zone, fault, and fracture (Figure 2). The brittle–ductile shear zone trends northeast, consistent with the regional Luang Prabang structural belt, and generally controls the overall output of the orebodies. The faults are secondary structures of the regional brittle–ductile shear zone and trend NNE or nearly S–N. They control the main intrusions and geological boundaries in the mining area. Gold orebodies normally occur within the faults and their secondary fractures.

Figure 2. Simplified geological map of the Sanakham gold deposit and geological cross-sections along line AA′.

The Middle Triassic intermediate–acid magmatic rocks are well developed and intruded into the Upper Carboniferous low-grade metamorphic rocks as an NNE-trending intrusive stock (Figure 2). The intrusions mainly consist of quartz monzodiorite with a hypidiomorphic granular texture and massive structure. It is composed of plagioclase,

amphibole, alkaline feldspar, a small amount of quartz, and trace amounts of pyrite in size of 0.1–4 mm, and is gray-white in color because of weathering.
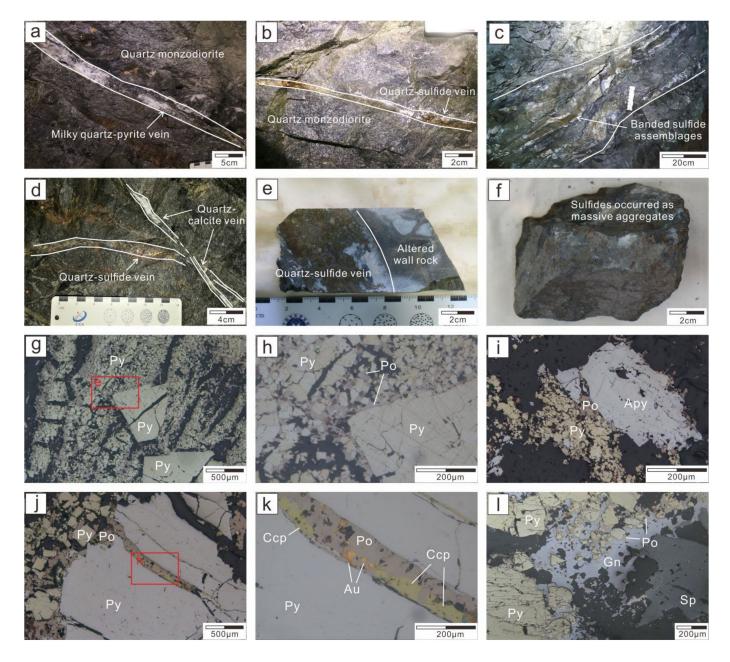
Ninety-one gold orebodies have been identified in the Sanakham deposit, and they can be divided into more than ten orebody groups (Figure 2). Most of the orebodies, vein or veinlet in shape, are included in the Au9 orebody group and account for 3/4 of the total gold resources. The several main orebodies in the Au9 orebody group are about 80–400 m in length, strike towards the NE, and dip 10°–40° SE with a depth of 300–600 m. They range in thickness from 0.8 to 4 m, averaging about 1.2–1.5 m. The gold grade ranges from 1.0 to 12.3 g/t, with an average gold grade of 3.05 g/t. The wallrocks are generally quartz monzonite, slate, and, locally hornfel.

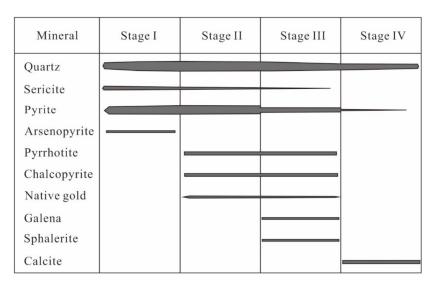### 2.3. Wall-Rock Alterations and Ore Mineralization

The wall-rock alteration at Sanakham mainly developed in the quartz monzodiorite and is controlled by the NE–NNE trending faults. The hydrothermal alterations are primarily silicification, sulfidation, sericitization, and carbonation, among which silicification and sulfidation have the closest relationship with gold mineralization. Silicification is the most widely distributed alteration, normally occurred as veins and networks, with a small amount disseminated in the intrusions. Sulfidation is dominated by pyrite, and lesser pyrrhotite, chalcopyrite, arsenopyrite, galena, and sphalerite. They co-exist with quartz to form quartz-sulfide veins (Figure 3a–d), generally as banded sulfide assemblages or massive aggregates (Figure 3e–f). The plagioclase, biotite, and potassium feldspar are locally subjected to sericitization around the orebodies, showing a coexistence relationship with disseminated silicification. Carbonation is normally in the form of calcite veinlets, 0.1 to 1 cm in width, interspersed in the wall rock. K-feldspar and chlorite are widely distributed in the intrusions and formed earlier than gold-related mineralization. Hydrothermal metasomatic alteration develops along the contact zones between quartz monzonite and slate, with a width of less than 20 m. It is characterized by skarnization, marbleization and hornfel alteration, but has little spatial relation with gold mineralization.

The lode gold orebodies primarily occur in the fault zones and fractures in the quartz monzodiorite and locally extend into Upper Carboniferous strata along with the structures. Primary sulfide ores mainly present vein stockwork and massive structures followed by disseminated structures. The ore minerals are primarily pyrite (~10 vol%), with lesser chalcopyrite and pyrrhotite (each 2–3 vol%), and a small amount of arsenopyrite, galena, and sphalerite (each ~1 vol%); the gangue minerals mainly consist of quartz (60–70 vol%) with minor calcite (5–10 vol%) and lesser sericite (1–3 vol%). Based on cross-cutting relationships and mineral assemblage characteristics (Figure 3), four mineralization stages have been identified in Sanakham (Figure 4): quartz–pyrite–arsenopyrite (stage I), quartz–pyrite–pyrrhotite-chalcopyrite (stage II), quartz–pyrite–base-metal sulfide (stage III), and quartz–carbonate (stage IV). Native gold occurs mainly in the main ore stages, i.e., stages II and III.

Stage I is normally quartz veins that comprise milky white quartz (Figure 3a), minor sericite, and euhedral to subhedral coarse-grained disseminated pyrite (Figure 3g) and arsenopyrite (Figure 3i). Stage II is characterized by quartz–sulfide veins and veinlets in grey color. The minerals are primarily subhedral to anhedral fine-grained pyrite, with minor pyrrhotite and chalcopyrite, which normally occurs around the boundary of stage I pyrite and arsenopyrite (Figure 3h,i). Native gold appears generally as irregular inclusions in pyrrhotite or chalcopyrite that fill in fractures of pyrite (Figure 3j,k). Similarly, stage III is characterized by quartz–sulfide veins and sulfide massive aggregations that consist of quartz, pyrite, pyrrhotite, chalcopyrite, and galena and sphalerite in particular (Figure 3l). They normally crosscut or overprint the stage II veins. Stage IV is characterized by quartz–calcite veinlets that crosscut the quartz–sulfide veins (Figure 3d).

Figure 3. Typical alteration and mineralization in the Sanakham gold deposit (**d**–**i** are reflected light images). (**a**), Milky quartz–pyrite vein in quartz monzodiorite; (**b**), quartz–sulfide vein in quartz monzodiorite; (**c**), banded sulfide assemblages; (**d**), quartz—calcite vein crosscut quartz—sulfide vein; (**e**), coexistence of sulfides and quartz in hand sample; (**f**), sulfides occurred as massive aggregates; (**g**,**h**), stage I euhedral to subhedral coarse-grained pyrite and stage II subhedral to anhedral fine-grained pyrite and pyrrhotite; (**i**), stage II pyrite and pyrrhotite occurred around stage I arsenopyrite; (**j**,**k**), native gold coexisting with pyrrhotite or chalcopyrite that fills in fractures of pyrite; (**l**), sulfide aggregations in stage III. Apy, arsenopyrite; Au, native gold; Ccp, chalcopyrite; Gn, galena; Po, pyrrhotite; Py, pyrite.

Mineral	Stage I	Stage II	Stage III	Stage IV
Quartz				
Sericite				
Pyrite				
Arsenopyrite				
Pyrrhotite				
Chalcopyrite				
Native gold				
Galena				
Sphalerite				
Calcite				

Figure 4. Paragenetic sequence of hydrothermal minerals in the Sanakham gold deposit, with line thickness indicating the relative abundance of minerals.

3. Sampling and Analytical Methods

A total of nine samples of gold-bearing ore were selected for fluid-inclusion analyses. Twenty doubly polished sections (about 0.1 mm thick) were chosen for petrographical study; of these, twelve sections were selected for microthermometry and Laser Raman study on hydrothermal quartz grains at the Fluid Inclusion Laboratories, Chengdu Center of China Geological Survey.

Fluid inclusion microthermometry was made with a Linkam THMSG 600 heating-cooling stage (-198 to $600\ ^{\circ}C$). The reproducibility of measurements was $\pm 1\ ^{\circ}C$ at temperatures $>30\ ^{\circ}C$ and $\pm\ 0.1\ ^{\circ}C$ at temperatures $<30\ ^{\circ}C$. The measurements of melting temperatures of ice ($T_{m\ ice}$), melting temperatures of the carbonic phase (mainly consist of CO_2 and CH_4, $T_{m\ carbon}$), clathrate-melting temperatures ($T_{m\ clath}$), and partial homogenization of carbonic phase ($T_{h\ carbon}$) were made at the heating rate of $0.2\ ^{\circ}C/min$, and for final homogenization temperature ($T_{h\ TOT}$), the heating rate was $1.0\ ^{\circ}C/min$.

Laser Raman spectroscopy of individual inclusions was performed using a Renishaw Raman spectrometer equipped with a 514 nm Ar ion laser as the source of excitation. The instrument records peaks in the range of 1200 to 3800 cm^{-1} with a resolution of $\pm 1\ cm^{-1}$ and a spectral repeatability of less than 0.1 cm^{-1}.

4. Results

4.1. Fluid-Inclusion Petrography

Based on micro-observation, microthermometry and Laser Raman analyses, the fluid inclusions were classified and grouped according to textural criteria using the FIA (fluid inclusion assemblage) method [20,21]. Three gold-related primary fluid inclusion types were observed in quartz: type *M*, CH_4-rich fluid inclusion; type *C*, CO_2-rich fluid inclusion; and type *W*, aqueous inclusions. Type *M* inclusions normally comprise a carbonic vapor phase and an aqueous phase at room temperature (Figure 5a). The carbonic phase consists primarily of CH_4, less of CO_2, and occasionally of C_2H_6 and H_2S, and separates into vapor and liquid carbonic phases through cooling (Figure 5b). These inclusions have a continuum V/(L + V) ratios range from 0.3 to 0.8 and homogenize to either liquid or vapor. Daughter minerals can be occasionally found in individual type *M* inclusions (Figure 5c). Type *C* inclusions contain two (aqueous + carbonic) or three (aqueous + liquid carbonic + vapor carbonic) phases at room temperature, and can be further divided into two subtypes based on their V/(L + V) ratios: type *C1* has V/(L + V) ratios mostly between 0.1 and 0.3 and homogenizes into liquid (the aqueous phase, Figure 5d), whereas type *C2* has V/(L + V) ratios of 0.6 and 0.9 and normally homogenizes into vapor (the carbonic phase, Figure 5e).

The carbonic phase of type *C* inclusions consists of major CO_2 and less CH_4, which is different from type *M* inclusions. Type *W* aqueous inclusions comprise an aqueous phase and a vapor phase with V/(L + V) ratios of 0.05 to 0.25, and homogenize to liquid (Figure 5f). The type *M* and *C* inclusions are normally 5–15 μm in diameter, have predominately regular to negative crystal shape or partly irregular shape. The type *W* inclusions are relatively smaller (2–10 μm) and have regular to irregular shape.

Six groups of FIA occur in hydrothermal quartz grains and are summarized in Table 1. Group 1 FIA consists of type *M* inclusions that show nearly constant V/(L + V) ratios, and widely distributed as clusters in stage I quartz (Figure 5g). Group 2 FIA, composed of *C1* inclusions sharing the same composition, locally occurs as clusters in stage II quartz (Figure 5h). Group 3 FIA consists of *M* and *C1* inclusions that widely occur as clusters in stage II quartz and show various volumes of the carbonic phases (Figure 5i). Group 4 FIA, also composed of *C1* inclusions sharing the same composition, exists in stage III quartz, either as clusters, or along pseudo-secondary trails, or as isolated inclusions (Figure 5j). Group 5 FIA is distinctive and widespread in stage III quartz and consists of type *C1* and *C2* inclusions. The coexisting *C1* and *C2* inclusions have different V/(L + V) ratios and homogenize to liquid and vapor, respectively (Figure 5k,l). Group 6 FIA generally occurred in stage IV quartz and was comprised of *W* inclusions with identical V/(L + V) ratios (Figure 5m).

Table 1. Summary of the fluid inclusion and FIA groups in hydrothermal quartz from four mineralization stages.
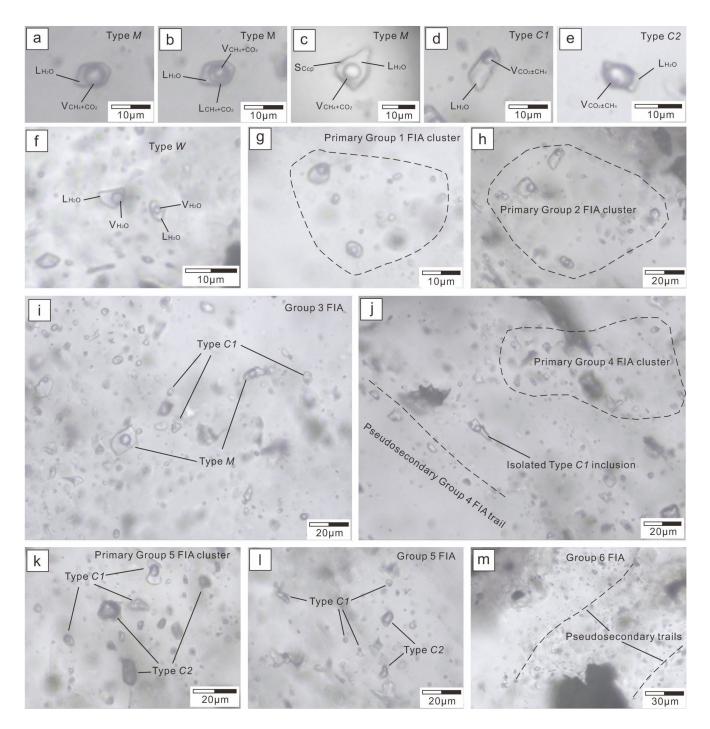
Ore Stage	FIA Group	Fluid Inclusion Type	Frequency of Occurrences	Implication For Ore Fluids Processes
Stage I	Group 1	*M*	Abundant	Homogeneous fluid
Stage II	Group 2	*C1*	Local	Homogeneous fluid
	Group 3	*M + C1*	Abundant	Fluid immiscibility
Stage III	Group 4	*C1*	Local	Homogeneous fluid
	Group 5	*C1 + C2*	Abundant	Fluid immiscibility
Stage IV	Group 6	*W*	Abundant	Homogeneous fluid

4.2. Results of Microthermometry

A total of 23 FIAs selected from hydrothermal quartz from all four stages were analyzed. The microthermometric data and calculated parameters (min, max, mean and number) for every FIA are listed in Tables 2–5. Of which, mean values of each type of fluid inclusions in every FIA are used for assessment and math statistics.

4.2.1. FIA in Stage I

Four Group 1 FIAs, each comprising 3–5 inclusions, were measured to gain exact microthermometry data (Table 2 and Figure 6). The $T_{m\,carbon}$ of type *M* inclusions occurs between −74.2 and −69.5 °C, with a mean value of −72.2 °C. The $T_{m\,clath}$ and $T_{h\,carbon}$ of type *M* inclusions range from −5.7 to −2.9 °C (mean −4.2 °C), and 4.9 to 9.5 °C (mean 6.8 °C), relatively. These inclusions generally homogenize into liquid phase finally, with $T_{h\,TOT}$ between 326° and 345 °C (mean 337 °C).

Figure 5. Photomicrographs of typical fluid inclusions and FIA groups in the Sanakham gold deposit. (**a**) Typical type *M* CH_4-rich fluid inclusion consisting of H_2O liquid and carbonic vapor ($CH_4 + CO_2 \pm C_2H_6 \pm H_2S$) phases at room temperature; (**b**) type *M* FI consisting of three (H_2O liquid + carbonic liquid + carbonic vapor) phases at about $-20°C$; (**c**) type *M* CH_4-rich fluid inclusion with daughter mineral (chalcopyrite); (**d**) type *C1* liquid-rich CO_2 inclusion; (**e**) type *C2* vapor-rich CO_2 inclusion; (**f**) type *W* two-phase H_2O-NaCl inclusion; (**g**) primary cluster of Group 1 FIA in stage I quartz; (**h**) primary cluster of Group 2 FIA in stage II quartz; (**i**) group 3 FIA in stage II quartz consisting of type *M* and *C1* inclusions with various volumes of the carbonic phases; (**j**) Group 4 FIA occurred as cluster, pseudo-secondary trail, and isolated type *C1* inclusions in stage III quartz; (**k**) primary cluster of Group 5 FIA consisting of type *C1* and *C2* inclusions showing opposite modes of homogenization at approximately the same temperature; (**l**) pseudo-secondary Group 5 FIA trail in stage III quartz; (**m**) pPseudo-secondary Group 6 FIA trails containing type *W* fluid inclusions in stage IV quartz.

Figure 6. Ranges of $T_{h\,TOT}$ (**a**), $T_{m\,carbon}$ (**b**), salinity (**c**), bulk density (**d**), bulk $X_{CO2} + X_{CH4}$ (**e**), and carbonic X_{CH4} (**f**) versus Groups 1–6 FIA in the four stages, respectively. The points in the middle of the bars are the mean value.

4.2.2. FIA in Stage II

Two Group 2 FIAs, which are comprised of four type *C1* inclusions each, were measured successfully (Table 3 and Figure 6). The $T_{m\,carbon}$, $T_{m\,clath}$, $T_{h\,carbon}$, and $T_{h\,TOT}$ of *C1* inclusions in Group 2 FIA are −57.9 to −57.5 °C (mean −57.7 °C), 4.3 to 4.8 °C (mean 4.6 °C), 18.2 to 20.3 °C (mean 19.3 °C), and 305 to 318 °C (mean 312 °C), respectively. The microthermometric data are similar to those in Group 1 FIA in stage I quartz.

Six Group 3 FIAs, which are widespread in stage II quartz and consist of several coexisting type *M* and *C1* inclusions, were chosen for microthermometry (Table 3 and Figure 6). The $T_{m\,carbon}$ of type *M* inclusions occurs between −72.0 and −64.0 °C (mean −68.4 °C), while the type *C1* inclusions have an obviously higher $T_{m\,carbon}$ range from −60.6 and −57.2 °C (mean −58.5 °C). The $T_{m\,clath}$ and $T_{h\,carbon}$ of type *M* inclusions range from −9.8 to −3.7 °C (mean −6.1 °C) and 4.3 to 16.2 °C (mean 9.7 °C), respectively. Similarly, the type *C1* inclusions have a higher $T_{m\,clath}$ and $T_{h\,carbon}$ range from 3.5 to 5.9 °C (mean 4.6 °C) and 16.4 to 23.3 °C (mean 19.5 °C), respectively. The *M* inclusions generally homogenize finally into the liquid phase with $T_{h\,TOT}$ between 288° and 355 °C (mean

327 °C). All of the type *C1* inclusions finally homogenize into the liquid phase and occur generally between 290° and 337°C, with a mean value of 322 °C.

Table 2. Summary of the microthermometric data and calculated parameters for Group 1 FIAs from stage I quartz.

FIA Group	FIA No.	FI Type	Range	$T_{m\ carbon}$ (°C)	$T_{m\ clath}$ (°C)	$T_{h\ carbon}$ (°C)	$T_{h\ TOT}$ (°C)	Salinity (wt.% NaCl)
Group 1	Group 1-1	*M*	Min	−76.1	−3.5	7.8	328	17.9
	(N = 5)		Max	−70.3	−2.2	11.1	352	19.1
			Mean	−74.2	−2.9	9.5	340	18.6
	Group 1-2	*M*	Min	−74.4	−4.7	3.1	336	18.8
	(N = 4)		Max	−71.1	−3.1	6.7	352	20.2
			Mean	−72.8	−3.9	4.8	345	19.5
	Group 1-3	*M*	Min	−73.5	−5.5	4.9	329	19.4
	(N = 4)		Max	−70.1	−3.8	8.2	346	20.9
			Mean	−71.6	−4.6	6.6	337	20.1
	Group 1-4	*M*	Min	−70.5	−7.4	5.2	317	19.8
	(N = 3)		Max	−68.7	−4.2	7.0	341	22.4
			Mean	−69.5	−5.7	6.0	326	21.0

4.2.3. FIA in Stage III

For the local existed Group 4 FIAs (Table 4 and Figure 6), the $T_{m\ carbon}$, $T_{m\ clath}$, $T_{h\ carbon}$, and $T_{h\ TOT}$ of type *C1* inclusions are, respectively, −57.2 to −57.0 °C (mean −57.1 °C), 4.3 to 5.0 °C (mean 4.7 °C), 22.0 to 23.3 °C (mean 22.7 °C), and 296 to 298 °C (mean 297 °C), which are generally similar to the Group 2 FIAs in stage II quartz.

The coexisting type *C1* and *C2* inclusions in the six measured Group 5 FIAs have the similar microthermometric data (Table 4 and Figure 6). The $T_{m\ carbon}$ of type *C1* inclusions occur between −58.8 and −56.8 °C, with a mean value of −57.7 °C. The type *C2* inclusions have slightly lower $T_{m\ carbon}$ range from −59.3 and −57.8 °C (mean −58.7 °C). The $T_{m\ clath}$ and $T_{h\ carbon}$ of type *C1* inclusions range relatively from 2.5 to 5.9 °C, and 16.9 to 24.0 °C. While, the type *C2* inclusions have slightly higher $T_{m\ clath}$ and $T_{h\ carbon}$ relatively from 4.9 to 6.4 °C, and 18.3 to 25.4 °C. The *C1* and *C2* inclusions finally homogenize into liquid and vapor phase, with $T_{h\ TOT}$ of 272° to 322 °C (mean 299 °C) and 278° to 339 °C (mean 304 °C), respectively. Some coexisting *C1* and *C2* inclusions have their V/(L + V) ratios change during heating, but cracked almost simultaneously before final homogenization.

4.2.4. FIA in Stage IV

Three Group 6 FIAs which comprise 4−5 type *W* inclusions in each were selected for microthermometry (Table 5 and Figure 6). The type *W* inclusions have melting temperatures of ice ($T_{m\ ice}$) range from −14.5 to −8.6 °C (mean −11.3 °C), and total homogenization into liquid occurs between 196 and 235 °C (mean 218 °C).

4.3. Results of Laser Raman Spectroscopy

Laser Raman spectroscopy indicates that both type *M* and type *C* fluid inclusions have carbonic component-dominate vapor phase (Figure 7). The gas phases of these inclusions consist of $CH_4 + CO_2 \pm C_2H_6 \pm H_2S$, with no detectable N_2. The type *C* inclusions normally have high CO_2 spectroscopic peaks (Figure 7a), while most spectroscopic analyses show high CH_4 peaks in type *M* inclusions (Figure 7b–d). Type *M* inclusions contain about 70–85 mole % CH_4 in carbonic phase, much higher than that of *C1* inclusions (CH_4 contents normally lower than 20%). The occasional daughter minerals in type *M* inclusions are normally chalcopyrite (Figure 7d) and calcite.

Table 3. Summary of the microthermometric data and calculated parameters for Groups 2 and 3 FIAs from stage II quartz.

FIA Group	FIA No.	FI Type	Range	$T_{m\ carbon}$ (°C)	$T_{m\ clath}$ (°C)	$T_{h\ carbon}$ (°C)	$T_{h\ TOT}$ (°C)	Salinity (wt.% NaCl)	Bulk Density (g/cm³)	XH_2O	$XNaCl$	$XCO_2 + XCH_4$	XCO_2	XCH_4
Group 2	Group 2-1	*C1*	Min	−58.6	3.9	16.5	295	9.4	0.782	0.825	0.026	0.051	0.046	0.005
	–	(N = 4)	Max	−57.2	4.8	20.6	314	10.7	0.983	0.915	0.034	0.148	0.144	0.004
			Mean	−57.9	4.3	18.2	305	10.1	0.877	0.872	0.030	0.098	0.092	0.006
	Group 2-2	*C1*	Min	−58.2	4.4	17.9	311	8.9	0.770	0.821	0.025	0.067	0.062	0.005
		(N = 4)	Max	−56.9	5.1	22.5	326	10.0	0.940	0.902	0.031	0.154	0.151	0.003
			Mean	−57.5	4.8	20.3	318	9.4	0.856	0.866	0.028	0.107	0.103	0.004
Group 3	Group 3-1	*M*	Min	−73.1	−11.0	0.3	324	23.0						
		(N = 4)	Max	−68.4	−8.3	8.9	347	25.0						
			Mean	−70.7	−9.8	4.3	335	24.1						
		C1	Min	−60.6	4.9	13.8	306	7.8	0.835	0.855	0.024	0.071	0.058	0.013
		(N = 3)	Max	−57.9	5.8	19.6	335	9.2	0.924	0.906	0.027	0.119	0.112	0.007
			Mean	−59.2	5.2	16.4	320	8.8	0.876	0.878	0.026	0.096	0.084	0.012
	Group 3-2	*M*	Min	−72.4	−8.2	2.1	341	21.7						
		(N = 3)	Max	−70.6	−6.6	7.6	364	23.0						
			Mean	−71.5	−7.5	5.0	355	22.4						
		C1	Min	−59.5	5.3	16.7	329	7.0	0.732	0.807	0.019	0.053	0.046	0.007
		(N = 3)	Max	−57.3	6.3	19.3	342	8.6	0.968	0.920	0.027	0.174	0.169	0.005
			Mean	−58.1	5.9	18.1	335	7.6	0.833	0.862	0.022	0.116	0.108	0.008
	Group 3-3	*M*	Min	−67.2	−4.3	14.8	315	18.6						
		(N = 3)	Max	−63.8	−2.9	17.9	339	19.8						
			Mean	−65.6	−3.7	16.2	326	19.3						
		C1	Min	−58.4	3.5	22.4	328	9.4	0.730	0.794	0.025	0.084	0.077	0.007
		(N = 4)	Max	−57.0	4.8	24.0	345	11.3	0.909	0.881	0.035	0.181	0.177	0.004
			Mean	−57.6	4.1	23.3	337	10.4	0.825	0.845	0.030	0.125	0.120	0.005
	Group 3-4	*M*	Min	−65.7	−6.8	12.7	273	20.6						
		(N = 4)	Max	−62.1	−5.2	13.9	306	21.9						
			Mean	−64.0	−5.9	13.3	288	21.2						
		C1	Min	−57.9	3.8	19.7	282	9.8	0.847	0.859	0.029	0.055	0.052	0.003
		(N = 3)	Max	−56.8	4.5	22.0	297	10.9	0.973	0.911	0.034	0.112	0.111	0.001
			Mean	−57.2	4.2	20.9	290	10.3	0.925	0.894	0.032	0.075	0.073	0.002
	Group 3-5	*M*	Min	−73.1	−6.2	8.8	325	20.4						
		(N = 3)	Max	−71.2	−4.9	13.7	346	21.4						
			Mean	−72.0	−5.5	11.2	336	20.9						
		C1	Min	−61.4	2.9	17.4	320	10.6	0.802	0.831	0.030	0.047	0.037	0.010
		(N = 2)	Max	−59.8	4.0	21.6	338	12.1	0.999	0.914	0.039	0.139	0.120	0.019
			Mean	−60.6	3.5	19.5	329	11.3	0.895	0.874	0.034	0.092	0.075	0.017

Table 3. *Cont.*

FIA Group	FIA No.	FI Type	Range	$T_{m\ carbon}$ (°C)	$T_{m\ clath}$ (°C)	$T_{h\ carbon}$ (°C)	$T_{h\ TOT}$ (°C)	Salinity (wt.% NaCl)	Bulk Density (g/cm³)	XH_2O	$XNaCl$	XCO_2 + XCH_4	XCO_2	XCH_4
	Group 3-6	*M*	Min	−68.9	−4.8	6.4	304	18.8						
		(N = 4)	Max	−64.7	−3.1	9.2	342	20.3						
			Mean	−66.6	−4.1	7.9	323	19.7						
		C1	Min	−58.8	4.4	16.3	311	8.5	0.752	0.812	0.023	0.065	0.059	0.007
		(N = 3)	Max	−57.2	5.4	20.8	334	10.0	0.946	0.904	0.031	0.165	0.160	0.005
			Mean	−58.1	4.9	18.8	322	9.2	0.853	0.865	0.027	0.108	0.100	0.008

Table 4. Summary of the microthermometric data and calculated parameters for Groups 4 and 5 FIAs from stage III quartz.
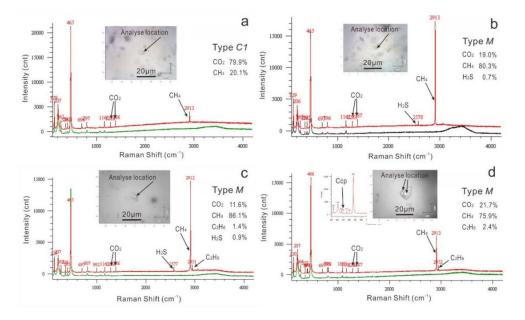
FIA Group	FIA No.	FI Type	Range	$T_{m\ carbon}$ (°C)	$T_{m\ clath}$ (°C)	$T_{h\ carbon}$ (°C)	$T_{h\ TOT}$ (°C)	Salinity (wt.% NaCl)	Bulk Density (g/cm³)	XH_2O	$XNaCl$	XCO_2 + XCH_4	XCO_2	XCH_4
Group 4	FIA 4-1	*C1*	Min	−57.4	3.8	22.1	286	9.7	0.851	0.862	0.029	0.068	0.065	0.003
		(N = 4)	Max	−56.8	4.6	24.2	308	10.9	0.941	0.898	0.034	0.110	0.109	0.001
			Mean	−57.0	4.3	23.3	298	10.1	0.885	0.876	0.030	0.093	0.091	0.002
	FIA 4-2	*C1*	Min	−57.7	4.6	19.6	293	8.6	0.796	0.838	0.024	0.066	0.063	0.003
		(N = 5)	Max	−56.7	5.3	24.4	301	9.7	0.941	0.904	0.030	0.138	0.137	0.001
			Mean	−57.2	5.0	22.0	296	9.1	0.865	0.872	0.027	0.101	0.098	0.003
Group 5	FIA 5-1	*C1*	Min	−58.2	2.0	14.2	266	11.7	0.901	0.873	0.036	0.041	0.038	0.003
		(N = 4)	Max	−56.6	3.2	19.6	279	13.3	1.021	0.916	0.043	0.091	0.091	0.000
			Mean	−57.3	2.5	17.1	272	12.6	0.974	0.901	0.040	0.059	0.057	0.002
		C2	Min	−60.1	3.8	16.3	270	9.5	0.860	0.399	0.013	0.332	0.279	0.053
		(N = 3)	Max	−57.9	4.7	22.4	287	10.9	0.884	0.644	0.024	0.588	0.553	0.035
			Mean	−59.0	4.3	19.1	278	10.1	0.872	0.539	0.019	0.443	0.394	0.049
	FIA 5-2	*C1*	Min	−59.2	5.6	19.5	307	7.1	0.832	0.865	0.021	0.059	0.052	0.007
		(N = 3)	Max	−57.1	6.2	23.2	325	8.1	0.949	0.916	0.025	0.115	0.112	0.003
			Mean	−58.3	5.9	21.3	316	7.6	0.893	0.893	0.023	0.084	0.077	0.007
		C2	Min	−59.5	6.0	18.7	302	6.1	0.827	0.336	0.007	0.382	0.332	0.050
		(N = 2)	Max	−58.1	6.8	20.1	334	7.5	0.875	0.603	0.015	0.657	0.611	0.046
			Mean	−58.8	6.4	19.4	318	6.8	0.850	0.489	0.011	0.500	0.450	0.050
	FIA 5-3	*C1*	Min	−57.2	3.3	22.9	313	10.4	0.812	0.838	0.030	0.046	0.045	0.001
		(N = 4)	Max	−56.6	4.1	25.3	329	11.6	0.998	0.917	0.037	0.132	0.132	0.000
			Mean	−56.8	3.7	24.0	322	11.0	0.900	0.879	0.034	0.088	0.087	0.001
		C2	Min	−58.6	4.5	23.5	334	9.2	0.830	0.517	0.016	0.276	0.251	0.025
		(N = 2)	Max	−57.2	4.9	27.3	345	9.8	0.866	0.700	0.024	0.467	0.453	0.014
			Mean	−57.9	4.7	25.4	339	9.5	0.847	0.620	0.020	0.360	0.338	0.022

Table 4. *Cont.*

FIA Group	FIA No.	FI Type	Range	$T_{m\ carbon}$ (°C)	$T_{m\ clath}$ (°C)	$T_{h\ carbon}$ (°C)	$T_{h\ TOT}$ (°C)	Salinity (wt.% NaCl)	Bulk Density (g/cm³)	XH_2O	XNaCl	XCO_2 + XCH_4	XCO_2	XCH_4
	FIA 5-4	C1	Min	−59.2	2.9	14.5	278	9.5	0.888	0.879	0.029	0.038	0.033	0.005
		(N = 4)	Max	−58.4	4.7	19.2	299	12.1	1.022	0.923	0.039	0.092	0.085	0.007
			Mean	−58.8	3.6	16.9	290	11.2	0.950	0.899	0.035	0.066	0.059	0.007
		C2	Min	−59.4	4.1	16.2	282	8.0	0.858	0.400	0.011	0.445	0.387	0.058
		(N = 2)	Max	−59.2	5.7	20.3	294	10.4	0.863	0.536	0.019	0.589	0.518	0.071
			Mean	−59.3	4.9	18.3	288	9.2	0.860	0.474	0.015	0.511	0.450	0.061
	FIA 5-5	C1	Min	−58.4	3.8	21.2	301	10.0	0.806	0.837	0.029	0.065	0.060	0.005
		(N = 2)	Max	−57.2	4.4	24.8	313	10.9	0.949	0.901	0.034	0.135	0.131	0.004
			Mean	−57.8	4.1	23.0	307	10.4	0.886	0.875	0.031	0.093	0.088	0.005
		C2	Min	−60.7	3.6	22.5	310	10.1	0.832	0.485	0.017	0.375	0.304	0.071
		(N = 3)	Max	−57.1	4.3	25.9	324	11.2	0.841	0.601	0.023	0.498	0.483	0.015
			Mean	−59.1	4.0	24.2	316	10.6	0.836	0.548	0.020	0.432	0.384	0.048
	FIA 5-6	C1	Min	−57.5	4.3	21.1	273	8.6	0.843	0.863	0.025	0.041	0.039	0.002
		(N = 4)	Max	−57.0	5.3	24.9	295	10.1	1.003	0.927	0.032	0.112	0.110	0.002
			Mean	−57.3	4.9	23.2	284	9.2	0.927	0.900	0.028	0.071	0.069	0.002
		C2	Min	−58.7	4.2	20.8	282	8.0	0.798	0.248	0.007	0.484	0.440	0.044
		(N = 3)	Max	−57.1	5.7	25.7	293	10.3	0.807	0.499	0.018	0.745	0.723	0.022
			Mean	−57.8	5.0	23.7	287	9.1	0.802	0.396	0.012	0.592	0.562	0.030

Table 5. Summary of the microthermometric data and calculated parameters for Group 6 FIAs from stage IV quartz.
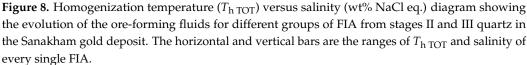
FIA Group	FIA No.	FI Type	Range	$T_{h\ TOT}$ (°C)	$T_{m\ ice}$ (°C)	Salinity (wt.% NaCl)	Bulk Density (g/cm³)	XH_2O	$XNaCl$
Group 6	Group 6-1	*W*	Min	227	−12.4	13.2	0.938	0.955	0.045
	(N = 4)		Max	243	−9.3	16.4	0.949	0.943	0.057
			Mean	235	−10.8	14.8	0.943	0.949	0.051
	Group 6-2	*W*	Min	215	−9.5	11.4	0.916	0.962	0.038
	(N = 5)		Max	232	−7.7	13.4	0.952	0.954	0.046
			Mean	223	−8.6	12.4	0.935	0.958	0.042
	Group 6-3	*W*	Min	184	−15.8	17.4	0.994	0.939	0.061
	(N = 4)		Max	206	−13.4	19.5	1.032	0.931	0.069
			Mean	196	−14.5	18.4	1.012	0.936	0.064

Figure 7. Laser Raman spectra of vapor bubbles (red color), aqueous (green color), or daughter minerals (in the **d** figure) of fluid inclusions in the Sanakham gold deposit. (**a**), Type *C1* inclusion; (**b**–**d**), type *M* inclusion.4.4. Composition and Density of Fluid Inclusions.

The salinity (wt% NaCl equiv (eq.)), bulk density, and composition of the above fluid inclusions were estimated according to the program of Bakker [22] using the software MacFlincor [23]. The CH_4 content in the carbonic phase of type *C* inclusions was estimated from the V-X phase diagram of the CO_2–CH_4 system [24]. The bulk CH_4 content, thus can be calculated combined with X_{CO2} + X_{CH4} and carbonic X_{CH4}. For the type *M* inclusions, CH_4 content is too high to get its accurate data based on the V-X phase diagram, thus evaluated by Laser Raman spectroscopy here. The salinities of type *M* inclusions are calculated using $T_{m\ clath}$ based on the equation from Darling et al. [25]. The bulk density of type *M* inclusions are hard to assess because of the high CH_4 content. The results of FIA assessment and math statistics are presented in Tables 2–5 and Figures 6 and 8.

Figure 8. Homogenization temperature ($T_{\text{h TOT}}$) versus salinity (wt% NaCl eq.) diagram showing the evolution of the ore-forming fluids for different groups of FIA from stages II and III quartz in the Sanakham gold deposit. The horizontal and vertical bars are the ranges of $T_{\text{h TOT}}$ and salinity of every single FIA.

4.3.1. Salinity

Stage I: Salinities in type *M* inclusions in Group 1 FIA vary from 18.6 to 21.0 wt% NaCl eq. (mean 9.8 wt% NaCl eq.).

Stage II: Salinities in type *C1* inclusions in Group 2 FIA vary from 9.4 to 10.1 wt% NaCl eq. (mean 9.8 wt% NaCl eq.). The type *C1* inclusions in Group 3 FIA that coexist with type *M* inclusions, similarly, have salinities ranging from 7.6 to 11.3 wt% NaCl eq. (mean 9.6 wt% NaCl eq.). Type *M* inclusions in Group 3 FIA, however, have higher salinities ranging from 19.3 to 24.1 wt% NaCl eq. (mean 21.3 wt% NaCl eq.), which are even higher than those in type *M* inclusions in Group 1 FIA.

Stage III: The range of salinities of types *C1* and *C2* inclusions in Group 5 FIAs are 6.8–10.6 wt% and 7.6–12.6 wt% NaCl eq. (mean 10.3, and 9.2 wt% NaCl eq.), respectively. The salinities of inclusions show a decreasing trend along with the increasing of CO_2 content in Group 5 FIAs. Salinities of type *C1* inclusions in Group 4 FIA are 9.1–10.1 NaCl eq. (mean 9.6 wt% NaCl eq.), basically equal to *C1* inclusions in Group 5 FIA in stage III, as well as *C1* inclusions in Group 2 FIA in stage II.

Stage IV: Type *W* inclusions in Group 6 FIA have relatively higher salinities of 12.4–18.4 NaCl eq. (mean 15.2 wt% NaCl eq.) than *C1* inclusions from previous stages.

4.3.2. Bulk Density

Stage II: The bulk densities of the type *C1* inclusions in both Groups 2 and 3 FIA are nearly the same, from 0.856–0.877 g/cm^3 (mean 0.867 g/cm^3) and 0.825–0.925 g/cm^3 (mean 0.868 g/cm^3), respectively.

Stage III: For Group 5 FIA, the bulk densities of the type *C1* and *C2* inclusions are quite different, with ranges of 0.886–0.974 g/cm^3 (mean 0.922 g/cm^3) and 0.802–0.872 g/cm^3 (mean 0.845 g/cm^3), respectively. Nevertheless, bulk densities of type *C1* inclusions in Group 4 FIA are 0.865–0.885 g/cm^3 (mean 0.875 g/cm^3), lower than the *C1* inclusions in Group 5 FIA in stage III but generally equal to *C1* inclusions in Group 2 FIA in stage II.

Stage IV: Bulk densities of *W* inclusions in Group 6 FIA are 0.935–1.012 g/cm^3 (mean 0.963 g/cm^3), obviously higher than the type *C* inclusions from the quartz of previous stages.

4.3.3. Content of CO_2 and CH_4

Both type *M* and *C* inclusions are able to assume the contents of CO_2 and CH_4. For type *M* inclusions, the content of $CO_2 + CH_4$ varies from 30 to 80 mol%, carbonic X_{CH4} of are generally 70–85 mole% based on Raman data.

In stage II, the type *C1* inclusions from Group 2 FIAs consist of ~87 mol% H_2O with $CO_2 + CH_4$ varying from 9.8 to 10.7 mol% (mean 10.3 mol%), while the type *C1* inclusions from Group 3 FIA that coexist with type *M* inclusions have similar bulk compositions, with a relatively wider $CO_2 + CH_4$ range of 7.5–12.5 mol% (mean 10.2 mol%). The carbonic X_{CH4} of type *C1* inclusions in Groups 2 and 3 FIAs are 4–6 mol% and 3–18 mol%, respectively. The bulk X_{CH4} of type *C1* inclusions in Groups 2 and 3 FIAs are therefore calculated to be 0.4–0.6 mol% (median 0.5 mol%) and 0.2–1.7 mol% (median 0.9 mol%), respectively.

In stage III, the $CO_2 + CH_4$ in type *C1* and *C2* inclusions from Group 5 FIAs have ranges of 5.9–9.3 mol% (median 7.7 mol%) and 36.0–59.2 mol% (median 47.3 mol%), respectively. The carbonic CH_4 and bulk CH_4 of *C2* inclusions are, respectively, 5–12 mol% and 2.2–6.1 mol%, higher than the coexisting *C1* inclusions (1–10 mol% and 0.1–0.7 mol%). Type *C1* inclusions in the two Group 4 FIAs have a higher content of $CO_2 + CH_4$ (9.3–10.1 mol%) than those in Group 5 FIA.
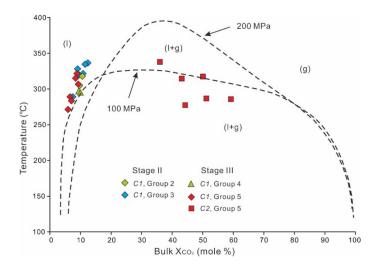
5. Discussion

5.1. Nature of Ore-Forming Fluids

According to fluid-inclusion petrography, Laser Raman spectroscopy, and microthermometry studies, there are big differences in composition among each fluid inclusion type and FIA group. Each of the Group 1, 2, 4, and 6 FIAs comprise only one type of fluid inclusion, and they represent a homogeneous fluid (Table 1). Group 1 FIA, consists of type *M* CH_4-rich fluid inclusions and represents a CH_4-rich CH_4–CO_2–NaCl–H_2O system in stage I, is characterized by medium temperatures (326–345 °C) and is CH_4-rich (~20–70% mol). Group 2 and 4 FIAs consist of type *C1* inclusions in stages II and III, respectively, belong to a NaCl–H_2O–CO_2–CH_4 system, with medium temperatures (296–318 °C) and medium salinity (9.1–10.1 wt% NaCl eq.), and are CO_2-rich (~10% mol) with minor CH_4 (~5% in carbonic phase). While Group 6 FIAs in stage IV belong to a NaCl–H_2O system, which is characterized by medium–low temperatures (196–239 °C) and relatively higher salinity (12.4–18.4 wt% NaCl eq.). Thus, the ore-forming fluids of Sanakham gold deposit might primarily belong to a medium temperature CH_4-rich CH_4–CO_2–NaCl–H_2O system, which evolved into a NaCl–H_2O–CO_2–CH_4 system in the main ore stage, and finally transformed into a medium–low temperature, medium–high salinity NaCl–H_2O fluid.

5.2. Fluid Immiscibility Processes

As mentioned above, both Group 3 FIAs in stage II and Group 5 FIAs in stage III consist of fluid inclusions with significantly different composition. The coexistence of the CH_4-rich and CO_2-rich inclusions (Group 3 FIA) and *C1* and *C2* inclusions with obviously different contents of CO_2 (Group 5 FIA) can be explained by the following three processes [26]: (1) fluid immiscibility caused by phase separation of a homogeneous fluid; (2) fluid mixing caused by heterogeneous trapping of multi-source hydrothermal fluids; or (3) post-entrapment modification. In this study, undeformed hydrothermal quartz grains with euhedral to subhedral shape are preferentially selected for fluid inclusion analysis. The inclusions for microthermometry, moreover, have no evidence of necking down [27]. The post-entrapment modification process thus can be excluded in Sanakham.

Ramboz et al. [28] propose three lines of evidence which may indicate a fluid immiscibility process for the two contrasting types of inclusions: (i) the two types of inclusions must occur in the same regions and there must be good evidence of contemporaneous trapping; (ii) the two types of inclusions must have similar total homogenization temperature ranges, with one type of inclusion homogenizing to the aqueous phase, and the others homogenizing to the vapor phase; (iii) if one inclusion type decrepitates before homogenization, then the other type must behave similarly. With reference to the above

principles, Group 5 FIA meets the criteria of fluid immiscibility, including (1) type *C1* and *C2* inclusions contemporaneously trapped in the same FIA (Figure 5k,l); (2) type *C1* and *C2* inclusions, respectively, homogenize to the aqueous phase (liquid) and CO_2 vapor phase, and have a similar $T_{h\,TOT}$ (272–322 °C and 278–339 °C; Table 4); (3) some coexisting *C1* and *C2* inclusions generally have moderate V/(L + V) ratios, decrepitate before homogenization, and are not recorded in the data sheet. In addition, type C1 inclusions have slightly higher salinities (7.6–12.6 wt% NaCl eq.) than type *C2* inclusions (6.8–10.6 wt% NaCl eq. Figure 7c), because salt is preferentially fractionated into the aqueous phase during phase separation [29]. It is inferred that the *C1* and *C2* inclusions in Group 5 FIA are two endmembers of unmixed fluids of a medium temperature, medium salinity, and CO_2-rich parent fluid (Figure 9). Considering the widespread Group 5 FIA in stage III quartz, fluid immiscibility was a dominant process for stage III mineralization.
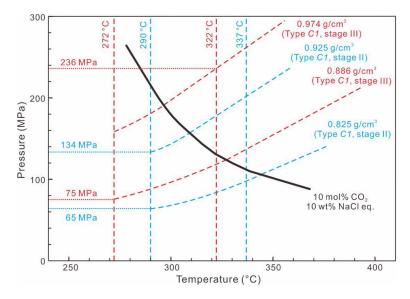

Figure 9. Homogenization temperature ($T_{h\,TOT}$) versus calculated equivalent mole fraction CO_2 of type *C1* and *C2* inclusions in stages II and III. The dashed curves delimit the two-phase regions of the H_2O–CO_2–NaCl system at 100 and 200 MPa, respectively. Data after Bowers and Helgeson (1983) [30]. g, gas; l, liquid.

For Group 3 FIA in stage II quartz, the contemporaneously trapped type *M* and *C1* inclusions also have similar homogenization temperature ranges (Figure 5i and Table 3), which are 288–355 °C and 290–337 °C, respectively. Except for the liquid phase, furthermore, type *M* and type *C1* inclusions have entirely different compositions in their carbonic phase. According to the Raman results, CH_4 contents in the carbonic phase of type *M* inclusions are ~80%, and the CO_2 contents are ~20%. Meanwhile, the type *C* inclusions contain contrary amounts of CO_2 and CH_4 (Figure 6), which can also be proven by their distinctly different $T_{m\,carbon}$ (Table 3). Thus, we cannot attribute the Group 3 FIA to a heterogeneous trapping of multi-source fluids led by fluid mixing [31], which prefers a continuum of compositions in diverse fluid inclusions. The type *M* and *C1* inclusions are better suggested to be two endmembers of unmixed fluids that belong to a CH_4-rich CH_4–CO_2–NaCl–H_2O system. The fluid immiscibility process should also take part in stage II mineralization in Sanakham.

5.3. Implications for Gold Deposition

Given that the native gold in Sanakham is closely associated with sulfides such as pyrite, pyrrhotite, and chalcopyrite, the ore fluids are considered to be near-neutral to weakly acidic [32,33]. The ore-forming fluids are < 400 °C and enriched in CO_2, indicating that the gold-transporting species were probably bisulfide complexes, mainly $Au(HS)_2^-$ [34,35]. Gold deposition, led by the destabilization of gold–bisulfide complexes, was likely associated with fluid immiscibility, fluid mixing, and other chemical changes [36,37].
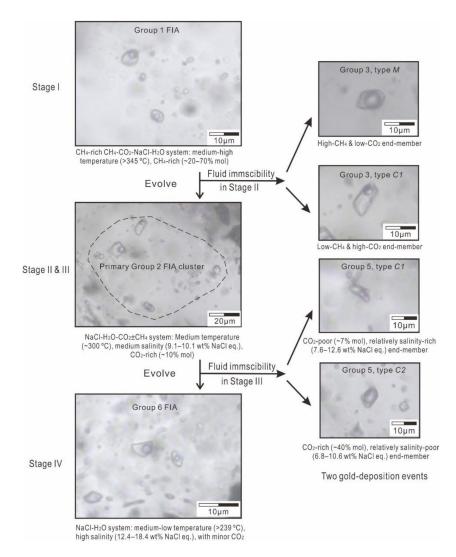
Taking into consideration the fluid immiscibility process in stages II and III, the Group 3 and 5 FIAs are reliable for estimating the P-T conditions of gold mineralization. The final homogenization temperatures of type *C1* inclusions, respectively, in Group 3 FIA (290–337 °C) and Group 5 FIA (272–322 °C) are considered to be close to the temperature of entrapment [20]. The P-T phase diagram (Figure 10) shows a representative solvus for H_2O–CO_2 fluids containing 10 wt% NaCl eq. and 10 mol% CO_2 (calculated after [30]), which is close to the composition of ore-forming fluids in stages II and III. The trapping pressures can be calculated from their isochores (0.825–0.925 g/cm^3 for stage II and 0.886–0.974 g/cm^3 for stage III) at the given homogenization temperatures. The estimated P-T conditions of gold mineralization in stages II and III ranged, respectively, from 134 to 65 MPa and 337 to 290 °C, and 236 to 75 Mpa and 322 to 272 °C (Figure 10). During fluid immiscibility caused by multiple hydraulic fracturing and pressure pulsation, gold deposition is believed to occur in conditions between lithostatic and hydrostatic pressure [38]. The highest and lowest pressures can be used to determine the depth considering that they are produced by the lithostatic and hydrostatic pressures, respectively. The densities of host quartz monzodiorite and ore-forming fluids are assumed, respectively, to be 2.7 g/cm^3 and 1.0 g/cm^3. Thus, for stage III, the calculated maximum and minimum depths are 8.7 km and 7.5 km, respectively. However, the highest pressure (134 MPa) in stage II indicates a depth of < 5.0 km, while the lowest pressure (65 MPa) indicates a depth of > 6.5 km. Taking the depth assumed from stage III into consideration, the depths for gold deposition in Sanakham are suggested to be 8.7–6.5 km. Fluid immiscibility in stage III occurred at relatively higher pressures than that in stage II, which might be attributed to a large release of CO_2 and subsequent pressure increase in the fracture system.

Figure 10. Estimated P-T conditions for the formation of the quartz veins in stages II and III in the Sanakham deposit. Representative isochores for mean bulk densities, respectively, for type *C1* inclusions, and the solvus for H_2O–CO_2 fluids containing 10 wt% NaCl eq. and 10 mol% CO_2 (calculated after reference [30]). The blue and red dashed lines define the range of $T_{h\ TOT}$ and bulk density of type *C1* inclusions in Groups 3 and 5 FIA, respectively. The dotted lines represent the range of trapping pressures.

Except for Group 3 and 5 FIAs, which show evidence for fluid immiscibility, the homogenization temperatures of other primary fluid inclusions could only be regarded as the minimum temperature of entrapment. Combined with the above discussion, thus, the evolution of ore-forming fluids and related gold-deposition processes can be summarized below (as shown in Figure 11). The primary ore-forming fluids in stage I belonged to a CH_4-rich CH_4–CO_2–NaCl–H_2O system (Group 1 FIA), which is characterized by medium–high temperature (>345 °C) and a high content of CH_4 (~20–70% mol). The first fluid

immiscibility process occurred in stage II and is represented by two coexisting endmembers (Group 3 FIA) including both those with high-CH_4 and low-CO_2 and the opposite. The ore fluids gradually evolved into a $NaCl–H_2O–CO_2 \pm CH_4$ fluid (Group 2 FIA) with medium temperature (~300 °C), medium salinity (9.1–10.1 wt% NaCl eq.), and a high content of CO_2 (~10% mol) during stages II and III. The second fluid immiscibility process occurred widely in stage III and therefore created two new coexisting endmembers (Group 5 FIA), which are the CO_2-poor (~7% mol) and relatively salinity-rich (7.6–12.6 wt% NaCl eq.) ones, as well as the opposite. Due to the volatile loss caused by fluid unmixing, the ore fluids finally evolved into a medium–low temperature (>239 °C), medium–high salinity (12.4–18.4 wt% NaCl eq.) $NaCl–H_2O$ system in stage IV (Group 6 FIA) accompanied by simply cooling. The two important gold-deposition events were generated, respectively, along with fluid immiscibility processes during stages II and III mineralization.

Figure 11. Evolution of ore-forming fluids and related gold-deposition processes in the Sanakham gold deposit.

Compared with important gold deposits in the Luang Prabang–Loei metallogenic belt, the epithermal gold class can be excluded in Sanakham because there is neither continental volcanic rock exposure, nor characteristic kaolinite, alunite, or porous silicification. Even though quartz monzodiorite predominates in the wall rock, the hydrothermal metasomatic alteration, such as skarnization and horny alteration, has little spatial relation with gold mineralization, different from the regional representative porphyry-skarn copper–gold deposits [15,17]. Actually, the lode-gold orebodies in Sanakham are strictly controlled

by the NE-NNE trending faults and crosscut the lithological interfaces between quartz monzodiorite and slate (Figure 2), which is similar to the Phapon epizonal orogenic gold deposit in the northern part of the Luang Prabang–Loei belt [13,14].

In most gold deposits, including porphyry and orogenic systems, the ore-forming fluids normally comprise remarkable contents of CO_2 which are closely related to the fluid immiscibility system. Additionally, it is not uncommon for methane to be included in the ore fluids, e.g., gold deposits from Jiaodong [39–45], Ailaoshan [46], West Qinling [47,48], and Southwest Guizhou [49] in China, the Abitibi gold belt in Canada [50], and Hamadi gold deposit in Sudan [51], as well as some porphyry Cu-Mo and rare-metal deposits [52–61]. Based on high P-T experimental results, Naden et al. [62] pointed out that the CH_4-bearing fluid system has a much wider immiscible area than the CO_2-bearing fluid system under the same P-T conditions. At 300 °C for example, the immiscibility process could occur when CO_2 content is higher than 15% mol, while the CH_4 content only needs to be above 5% mol [63]. Thus, a small amount of CH_4 in a $NaCl–H_2O–CO_2$ system could greatly expand the immiscibility area and result in gold deposition, which is identical to the stage II mineralization in Sanakham. However, the CH_4-rich $CH_4–CO_2–NaCl–H_2O$ ore fluids cannot be simply interpreted as products of alternative magmatic, metamorphic, or mantle-derived fluids. It is generally assumed that the extremely high content of CH_4 has an organic source, including partial decomposition of organic matter, or a reaction between water and graphite or organic carbon in the formations [64]. The Upper Carboniferous carbonaceous slate, therefore, might be a possible source of the abundant CH_4, even though more refined studies on the source and evolution of ore-forming fluids are further needed.

6. Conclusions

The Sanakham gold deposit, located in the Luang Prabang–Loei metallogenic belt, predominately consists of auriferous quartz vein-type orebodies that are controlled by NE-NNE trending faults within Middle Triassic quartz monzodiorite and secondary Upper Carboniferous low-grade metamorphic rocks. Detailed study through petrography, microthermometry, and Laser Raman spectroscopy on fluid inclusions in gold-related quartz were carried out in the Sanakham gold deposit. The following conclusions are drawn from this study on the evolution of ore-forming fluids and gold deposition mechanisms in Sanakham:

(1) Four mineralization stages have been distinguished in Sanakham, of which the quartz–pyrite–pyrrhotite-chalcopyrite stage (II) and the quartz–pyrite–base-metal sulfide stage (III) are identified as the main gold deposition stages.

(2) The initial ore-forming fluids belonged to a medium-high temperature CH_4-rich $CH_4–CO_2–NaCl–H_2O$ system, which gradually evolved into a medium temperature, medium salinity, and high CO_2 content $NaCl–H_2O–CO_2 \pm CH_4$ system during the main ore stages, and then a medium-low temperature, medium-high salinity $NaCl–H_2O$ system in stage IV.

(3) Gold-deposition events were generated along with the two fluid immiscibility processes during stage II and III mineralization, respectively. The former created two coexisting high-CH_4 and low-CO_2 and low-CH_4 and high-CO_2 endmembers, while the latter created two coexisting CO_2-poor and CO_2-rich endmembers.

(4) The presence of CH_4 in ore-forming fluids promoted the fluid immiscibility and resulted in gold deposition at P–T conditions generally around 236 to 65 MPa and 337 to 272 °C, with estimated gold mineralization depths of 8.7–6.5 km.

Author Contributions: Conceptualization, S.L. and L.G.; data curation, S.L., S.X. and H.L.; formal analysis, L.G. and J.D.; funding acquisition, S.L., L.G. and L.H.; investigation, L.G., M.S., F.N. and X.C.; writing—original draft, S.L.; writing—review and editing, L.G. and J.D. All authors have read and agreed to the published version of the manuscript.

Conflicts of Interest: The authors declare that they have no known competing financial interests or personal relationships that could have appeared to influence the work reported in this paper.

References

1. Liu, S.S.; Yang, Y.F.; Guo, L.N.; Nie, F.; Peng, Z.M.; Pan, G.T. Tectonic characteristics and metallogeny in Southeast Asia. *Geol. China* **2018**, *45*, 863–889. (In Chinese with English abstract)
2. Goldfarb, R.J.; Taylor, R.D.; Collins, G.S.; Goryachev, N.A.; Orlandini, O.F. Phanerozoic continental growth and gold metallogeny of Asia. *Gondwana Res.* **2014**, *25*, 48–102. [CrossRef]
3. Khin, Z.; Meffre, S.; Lai, C.K.; Santosh, M.; Burrett, C.F.; Graham, I.T.; Manaka, T.; Salam, A.; Kamvong, T.; Cromie, P. Tectonics and metallogeny of mainland Southeast Asia–A review and contribution. *Gondwana Res.* **2014**, *26*, 5–30. [CrossRef]
4. Wang, Y.J.; Yang, T.X.; Zhang, Y.Z.; Qian, X.; Gan, C.S.; Wang, Y.K.; Wang, Y.; Vongpaseuth, S. Late Paleozoic back-arc basin in the Indochina block: Constraints from the mafic rocks in the Nan and Luang Prabang tectonic zones, Southeast Asia. *J. Asian Earth Sci.* **2020**, *195*, 104333. [CrossRef]
5. Shi, M.F.; Khin, Z.; Liu, S.S.; Xu, B.C.; Meffre, S.; Cong, F.; Nie, F.; Peng, Z.M.; Wu, Z.B. Geochronology and petrogenesis of Carboniferous and Triassic volcanic rocks in NW Laos: Implications for the tectonic evolution of the Loei Fold Belt. *J. Asian Earth Sci.* **2021**, *208*, 104661. [CrossRef]
6. Qian, X.; Feng, Q.L.; Yang, W.Q.; Wang, Y.J.; Chonglakmani, C.; Monjai, D. Arc-like volcanic rocks in NW Laos: Geochronological and geochemical constraints and their tectonic implications. *J. Asian Earth Sci.* **2015**, *98*, 342–357. [CrossRef]
7. Qian, X.; Feng, Q.L.; Wang, Y.J.; Chonglakmani, C.; Monjai, D. Geochronological and geochemical constraints on the mafic rocks along the Luang Prabang zone: Carboniferous back-arc setting in northwest Laos. *Lithos* **2016**, *245*, 60–75. [CrossRef]
8. Rossignol, C.; Bourquin, S.; Poujol, M.; Hallot, E.; Dabard, M.-P.; Nalpas, T. The volcaniclastic series from the Luang Prabang Basin, Laos: A witness of a Triassic magmatic arc? *J. Asian Earth Sci.* **2016**, *12*, 159–183. [CrossRef]
9. Shi, M.F.; Wu, Z.B.; Liu, S.S.; Peng, Z.M.; Guo, L.N.; Nie, F.; Xu, S.W. Geochronology and petrochemistry of volcanic rocks in the Xaignabouli area, NW Laos. *J. Earth Sci.* **2019**, *30*, 37–51. [CrossRef]
10. Guo, L.N.; Hou, L.; Nie, F.; Liu, S.S.; Xu, S.W.; Zhang, Q.M. Zircon U-Pb dating of quartz-diorite from Luang Prabang tectonic belt in Laos: Implication for eastward subduction of the Paleo-Tethys Ocean. *Sediment. Geol. and Tethyan Geol.* **2020**, *40*, 68–75, (In Chinese with English abstract).
11. Blanchard, S.; Rossignol, C.; Bourquin, S.; Dabard, M.P.; Hallot, E.; Nalpas, T.; Poujol, M.; Battail, B.; Jalil, N.E.; Steyer, J.S.; et al. Late Triassic volcanic activity in South-East Asia: New stratigraphical, geochronological and paleontological evidence from the Luang Prabang Basin (Laos). *J. Asian Earth Sci.* **2013**, *70–71*, 8–26. [CrossRef]
12. Qian, X.; Feng, Q.L.; Wang, Y.J.; Yang, W.Q.; Chonglakmani, C.; Monjai, D. Petrochemistry and Tectonic Setting of the Middle Triassic Arc-Like Volcanic Rocks in the Sayabouli Area, NW Laos. *J. Earth Sci.* **2016**, *27*, 365–377. [CrossRef]
13. Liu, S.S. Study on the Tectonics-Magmatic-Mineralization of the Luang Prabang-Loei Copper-Gold Metallogenic Belt. Ph.D. Thesis, Chengdu Univerisity of Technology, Chengdu, China, 2021.
14. Kamvong, T.; Khin, Z. The origin and evolution of skarn-forming fluids from the Phu Lon deposit, northern Loei Fold Belt, Thailand. Evidence from fluid inclusion and sulfur isotope studies. *J. Asian Earth Sci.* **2009**, *34*, 624–633. [CrossRef]
15. Nie, F.; Liu, S.S.; Yang, Y.F.; Peng, Z.M.; Guo, L.N. Zircon U-Pb dating of the diorite of Phu Lon skarn Cu-Au deposit in Thailand and its significance. *Sediment. Geol. Tethyan Geol.* **2019**, *39*, 71–78. (In Chinese with English abstract)
16. Salam, A.; Khin, Z.; Meffre, S.; McPhie, J.; Lai, C.K. Geochemistry and geochronology of epithermal Au-hosted Chatree volcanic sequence: Implication for tectonic setting of the Loei Fold Belt in central Thailand. *Gondwana Res.* **2014**, *26*, 198–217. [CrossRef]
17. Guo, L.N.; Hou, L.; Liu, S.S.; Nie, F. REE geochemistry and C-O isotope characteristics of hydrothermal calcites: Implications for fluid–rock reaction and ore-forming processes in the Phapon gold deposit, NW Laos. *Minerals* **2018**, *8*, 438. [CrossRef]
18. Guo, L.N.; Liu, S.S.; Hou, L.; Wang, J.T.; Zhang, Q.M.; Shi, M.F.; Nie, F.; Yang, Y.F.; Peng, Z.M. Fluid inclusion and C-H-O isotopes geochemistry of the Phapon gold deposit, NW Laos: Implications for fluid source and ore genesis. *J. Earth Sci.* **2019**, *30*, 80–94. [CrossRef]
19. Zhao, Y.P.; Kang, T.S.; Ning, G.C.; Ge, H.; Pan, H. Geochemical characteristics of the volcanic intrusive complex in the Pangkuam copper-gold deposit of Laos and its geological significance. *Acta Petrol. Et Mineral.* **2017**, *36*, 281–294. (In Chinese with English abstract)
20. Goldstein, R.H.; Reynolds, T.J. *Systematics of Fluid Inclusions in Diagenetic Minerals*; SEPM Short Course 31; SEPM Society for Sedimentary Geology: Tulsa, OK, USA, 1994; Volume 31, pp. 1–199.
21. Chi, G.X.; Diamond, L.W.; Lu, H.Z.; Lai, J.Q.; Chu, H.X. Common problems and pitfalls in fluid inclusion study: A review and discussion. *Minerals* **2021**, *11*, 7. [CrossRef]

22. Bakker, R.J. Package Fluids 1. Computer programs for analysis of fluid inclusion data and for modelling bulk fluid properties. *Chem. Geol.* **2003**, *194*, 3–23. [CrossRef]

23. Brown, P.E.; Hagemann, S.G. MacFlincor and its application to fluids in Archaean lode-gold deposits. *Geochim. Cosmochim. Acta* **1995**, *59*, 3943–3952. [CrossRef]

24. Thiéry, R.; Vidal, J.; Dubessy, J. Phase equilibria modelling applied to fluid inclusions: Liquid-vapour equilibria and calculation of the molar volume in the CO_2-CH_4-N_2 system. *Geochim. Cosmochim. Acta* **1994**, *58*, 1073–1082. [CrossRef]

25. Darling, R.S. An extended equation to calculate NaCl contents from final clathrate melting temperatures in H_2O-CO_2-NaCl fluid inclusions: Implications for P-T isochore location. *Geochim. Cosmochim. Acta* **1991**, *55*, 3869–3871. [CrossRef]

26. Pichavant, M.; Ramboz, C.; Weisbrod, A. Fluid immiscibility in natural processes: Use and misuse: I. Phase equilibria analysis–a theoretical and geometrical approach. *Chem. Geol.* **1982**, *37*, 29–48.

27. Bakker, R.J.; Jansen, J.B.H. A mechanism for preferential H_2O leakage from fluid inclusions in quartz, based on TEM observations. *Contrib. Mineral. Petrol.* **1994**, *116*, 7–20. [CrossRef]

28. Ramboz, C.; Pichavant, M.; Weisbrod, A. Fluid immiscibility in natural processes: Use and misuse of fluid inclusion data, II. Interpretation of fluid inclusion data in terms of immiscibility. *Chem. Geol.* **1982**, *37*, 29–48. [CrossRef]

29. Lawrence, D.M.; Treloar, P.J.; Rankin, A.H.; Boyce, A.; Harbidge, P. A fluid inclusion and stable isotope study at the Loulo mining district, Mali, West Africa: Implications for multifluid sources in the generation of orogenic gold deposits. *Econ. Geol.* **2013**, *180*, 229–257. [CrossRef]

30. Bowers, T.S.; Helgeson, H.C. Calculation of thermodynamic and geochemical consequences of nonideal mixing in the system H_2O–CO_2–NaCl on phase relations in geologic systems: Equation of state for H_2O–CO_2–NaCl fluids at high pressures and temperatures. *Geochim. Cosmochim. Acta* **1983**, *47*, 1247–1275. [CrossRef]

31. Anderson, M.R.; Rankin, A.H.; Spiro, B. Fluid mixing in the generation of mesothermal gold mineralization in the Transvaal Sequence, Transvaal, South Africa. *Eur. J. Mineral.* **1992**, *4*, 933–948. [CrossRef]

32. Williams-Jones, A.E.; Bowell, R.J.; Migdisov, A.A. Gold in solution. *Elements* **2009**, *5*, 281–287. [CrossRef]

33. Guo, L.N.; Goldfarb, R.J.; Wang, Z.L.; Li, R.H.; Chen, B.H.; Li, J.L. A comparison of Jiaojia- and Linglong-type gold deposit ore-forming fluids: Do they differ? *Ore Geol. Rev.* **2017**, *88*, 511–533. [CrossRef]

34. Benning, L.G.; Seward, T.M. Hydrosulphide complexing of gold (I) in hydrothermal solutions from 150 to 500°C and 500 to 1500 bars. *Geochim. Cosmochim. Acta* **1996**, *60*, 1849–1871. [CrossRef]

35. Phillips, G.N.; Evans, K.A. Role of CO_2 in the formation of gold deposits. *Nature* **2004**, *429*, 860–863. [CrossRef] [PubMed]

36. Mikucki, E.J. Hydrothermal transport and depositional processes in Archean lode-gold systems: A review. *Ore Geol. Rev.* **1998**, *13*, 307–321. [CrossRef]

37. Pokrovski, G.S.; Tagirov, B.R.; Schott, J.; Hazemann, J.L.; Proux, O. A new view on gold speciation in sulfur-bearing hydrothermal fluids from in situ X-ray absorption spectroscopy and quantum-chemical modeling. *Geochim. Cosmochim. Acta* **2009**, *73*, 5406–5427. [CrossRef]

38. Weatherley, D.K.; Henley, R.W. Flash vaporization during earthquakes evidenced by gold deposits. *Nat. Geosci.* **2013**, *6*, 294–298. [CrossRef]

39. Fan, H.R.; Zhai, M.G.; Xie, Y.H.; Yang, J.H. Ore-forming fluids associated with granite-hosted gold mineralization at the Sanshandao deposit, Jiaodong gold province, China. *Mineral. Depos.* **2003**, *38*, 739–750. [CrossRef]

40. Deng, J.; Yang, L.Q.; Groves, D.I.; Zhang, L.; Qiu, K.F.; Wang, Q.F. An integrated mineral system model for the gold deposits of the giant Jiaodong province, eastern China. *Earth-Sci. Rev.* **2020**, *208*, 103274. [CrossRef]

41. Deng, J.; Qiu, K.F.; Wang, Q.F.; Goldfarb, R.J.; Yang, L.Q.; Zi, J.W.; Geng, J.Z.; Ma, Y. In-situ dating of hydrothermal monazite and implications on the geodynamic controls of ore formation in the Jiaodong gold province, Eastern China. *Econ. Geol.* **2020**, *115*, 671–685. [CrossRef]

42. Goldfarb, R.J.; Mao, J.W.; Qiu, K.F.; Goryachev, N. The great Yanshanian metallogenic event of eastern Asia: Consequences from one hundred million years of plate margin geodynamics. *Gondwana Res.* **2021**, *100*, 223–250. [CrossRef]

43. Qiu, K.F.; Goldfarb, R.J.; Deng, J.; Yu, H.C.; Gou, Z.Y.; Ding, Z.J.; Wang, Z.K.; Li, D.P. Gold deposits of the Jiaodong Peninsula, eastern China. *SEG Spec. Publ.* **2020**, *23*, 753–773.

44. Guo, L.N.; Deng, J.; Yang, L.Q.; Wang, Z.L.; Wang, S.R.; Wei, Y.J.; Chen, B.H. Gold deposition and resource potential of the Linglong gold deposit, Jiaodong Peninsula: Geochemical comparison of ore fluids. *Ore Geol. Rev.* **2020**, *120*, 103434. [CrossRef]

45. Song, M.C.; Xue, G.Q.; Liu, H.B.; Li, Y.X.; He, C.Y.; Wang, H.J.; Wang, B.; Song, Y.X.; Li, S.Y. A Geological-Geophysical Prospecting Model for Deep-Seated Gold Deposits in the Jiaodong Peninsula, China. *Minerals* **2021**, *11*, 1393. [CrossRef]

46. Li, Y.; Wang, D.; Wang, C.; Sun, Y.; Pu-chi, M. Geology and Geochemistry of Selected Gold Deposits in the Ailaoshan Metallogenic Belt, China: Origin of Ore-Forming Fluids. *Minerals* **2021**, *11*, 1276. [CrossRef]

47. Qiu, K.F.; Yu, H.C.; Deng, J.; McIntire, D.; Gou, Z.Y.; Geng, J.Z.; Chang, Z.S.; Zhu, R.; Li, K.N.; Goldfarb, R.J. The giant Zaozigou orogenic Au-Sb deposit in West Qinling, China: Magmatic or metamorphic origin? *Miner. Depos.* **2020**, *55*, 345–362. [CrossRef]

48. Yang, L.Q.; Deng, J.; Dilek, Y.; Qiu, K.F.; Ji, X.Z.; Li, N.; Taylor, R.D.; Yu, J.Y. Structure, geochronology, and petrogenesis of the Late Triassic Puziba granitoid dikes in the Mianlue suture zone, Qinling Orogen, China. *Geol. Soc. Am. Bull.* **2015**, *11/12*, 1831–1854. [CrossRef]

49. Peng, Y.W.; Gu, X.X.; Liu, L.; Cheng, W.B.; Zhang, Y.M.; Wu, C.Y.; Lv, P.R. Fluid inclusion characteristics and implications to mineralization in the Zimudang gold deposit in Southwest Guizhou Province, China. *Acta Mineral. Sin.* **2012**, *32*, 211–220, (In Chinese with English abstract).

50. Robert, F.; Kelly, W.C. Ore-forming fluids in Archean gold-bearing quartz veins at the Sigma Mine, Abitibi greenstone belt, Quebec, Canada. *Econ. Geol.* **1987**, *82*, 1464–1482. [CrossRef]

51. Xu, J.H.; Wang, J.X.; Xiang, P.; Li, Y.H.; Xiao, X.; Zhang, H.; Cheng, X.H. Extremely CO_2-rich fluid inclusions in an orogenic gold deposit: Hamadi gold deposit of Sudan. *Acta Petrol. Sin.* **2015**, *31*, 1040–1048. (In Chinese with English abstract)

52. He, D.Y.; Qiu, K.F.; Santosh, M.; Yu, H.C.; Long, Z.Y.; Wang, J.Y. Inhomogeneous crust-mantle interaction and Triassic tectonic escape of a Proterozoic microplate: A tale of the Bikou Terrane. *Lithos* **2021**, *396–397*, 106227. [CrossRef]

53. Qiu, K.F.; Deng, J.; Yu, H.C.; Wu, M.Q.; Wang, Y.; Zhang, L.; Goldfarb, R. Identifying hydrothermal quartz vein generations in the Taiyangshan porphyry Cu-Mo deposit (West Qinling, China) using cathodoluminescence, trace element geochemistry, and fluid inclusions. *Ore Geol. Rev.* **2021**, *128*, 103882. [CrossRef]

54. Qiu, K.F.; Taylor, R.D.; Song, Y.H.; Yu, H.C.; Song, K.R.; Li, N. Geologic and geochemical insights into the formation of the Taiyangshan porphyry copper–molybdenum deposit, Western Qinling Orogenic Belt, China. *Gondwana Res.* **2016**, *35*, 40–58. [CrossRef]

55. Wang, Y.; Qiu, K.F.; Müller, A.; Hou, Z.L.; Zhu, Z.H.; Yu, H.C. Machine Learning Prediction of Quartz Forming-Environments. *J. Geophys. Resour. Solid Earth* **2021**, *126*, e2021jb021925. [CrossRef]

56. Qiu, K.F.; Yu, H.C.; Hetherington, C.; Huang, Y.Q.; Yang, T.; Deng, J. Tourmaline composition and boron isotope signature as a tracer of magmatic-hydrothermal processes. *Am. Miner.* **2021**, *106*, 1033–1044. [CrossRef]

57. Qiu, K.F.; Yu, H.C.; Wu, M.Q.; Geng, J.Z.; Ge, X.K.; Gou, Z.Y.; Taylor, R.D. Discrete Zr and REE mineralization of the Baerzhe rare-metal deposit, China. *Am. Miner.* **2019**, *104*, 1487–1502. [CrossRef]

58. Wu, M.Q.; Samson, I.M.; Qiu, K.F.; Zhang, D.H. Concentration mechanisms of REE-Nb-Zr-Be mineralization in the Baerzhe deposit, NE China: Insights from textural and chemical features of amphibole and rare-metal minerals. *Econ. Geol.* **2021**, *116*, 651–679. [CrossRef]

59. Yu, H.C.; Qiu, K.F.; Hetherington, C.J.; Chew, D.; Huang, Y.Q.; He, D.Y.; Geng, J.Z.; Xian, H.Y. Apatite as an alternative petrochronometer to trace the evolution of magmatic systems containing metamict zircon. *Contrib. Mineral. Petrol.* **2021**, *176*, 68. [CrossRef]

60. Yu, H.C.; Qiu, K.F.; Pirajno, F.; Zhang, P.C.; Dong, W.Q. Revisiting Phanerozoic evolution of the Qinling Orogen (East Tethys) with perspectives of detrital zircon. *Gondwana Res.* **2021**, *accepted*. [CrossRef]

61. Zhang, L.; Qiu, K.F.; Hou, Z.L.; Pirajno, F.; Shivute, E.; Cai, Y.W. Fluid-rock reactions of the Triassic Taiyangshan porphyry Cu-Mo deposit (West Qinling, China) constrained by QEMSCAN and iron isotope. *Ore Geol. Revi.* **2021**, *132*, 104068. [CrossRef]

62. Naden, J.; Shepherd, T.J. Role of methane and carbon dioxide in gold depositions. *Nature* **1989**, *342*, 793–795. [CrossRef]

63. Van den Kerkhof, A.M.; Thiéry, R. Carbonic inclusions. *Lithos* **2001**, *55*, 49–68. [CrossRef]

64. Jiang, N.; Wang, Y.L. The role of CH_4 in gold mineralization. *Global Geol.* **1995**, *14*, 29–32. (In Chinese)